



Since January 2020 Elsevier has created a COVID-19 resource centre with free information in English and Mandarin on the novel coronavirus COVID-19. The COVID-19 resource centre is hosted on Elsevier Connect, the company's public news and information website.

Elsevier hereby grants permission to make all its COVID-19-related research that is available on the COVID-19 resource centre - including this research content - immediately available in PubMed Central and other publicly funded repositories, such as the WHO COVID database with rights for unrestricted research re-use and analyses in any form or by any means with acknowledgement of the original source. These permissions are granted for free by Elsevier for as long as the COVID-19 resource centre remains active.



# Crystal structure, chemical reactivity, kinetic and thermodynamic studies of new ligand derived from 4-hydroxycoumarin: Interaction with SARS-CoV-2



Chafia Ait-Ramdane-Terbouche<sup>a</sup>, Hasnia Abdeldjebar<sup>a</sup>, Achour Terbouche<sup>a,\*</sup>, Houria Lakhdari<sup>a</sup>, Khaldoun Bachari<sup>a</sup>, Thierry Roisnel<sup>b</sup>, Didier Hauchard<sup>c</sup>

<sup>a</sup> Centre de Recherche Scientifique et Technique en Analyses Physico-chimiques(CRAPC), BP384, Bou-Ismail, RP 42004, Tipasa, Algeria

<sup>b</sup> Univ Rennes- CNRS- ISCR (Institut des Sciences Chimiques de Rennes)-UMR 6226 F-35000 Rennes France

<sup>c</sup> Univ Rennes- Ecole Nationale Supérieure de Chimie de Rennes- CNRS- ISCR (Institut des Sciences Chimiques de Rennes)-UMR 6226 F-35000 Rennes France

## ARTICLE INFO

### Article history:

Received 12 May 2020

Revised 30 June 2020

Accepted 15 July 2020

Available online 16 July 2020

### Keywords:

Coumarin derivative

Crystal structure

Chemical reactivity

Thermodynamic properties

Interaction SARS-CoV-2/Mpro-L<sub>TA</sub>

## ABSTRACT

Currently, Covid-19 pandemic infects staggering number of people around the globe and causes a high rate of mortality. In order to fight this disease, a new coumarin derivative ligand (4-[(pyridin-3-ylmethyl)amino]-2H-chromen-2-one) (L<sub>TA</sub>) has been synthesized and characterized by single-crystal X-ray diffraction, NMR, ATR, UV-Visible and cyclic voltammetry. Chemical reactivity, kinetic and thermodynamic studies were investigated using DFT method. The possible binding mode between L<sub>TA</sub> and Main protease (Mpro) of SARS-CoV-2 and their reactivity were studied using molecular docking simulation.

Single crystal X-ray diffraction showed that L<sub>TA</sub> crystallizes in a monoclinic system with P2<sub>1</sub> space group. The reactivity descriptors such as nucleophilic index confirm that L<sub>TA</sub> is more nucleophile, inducing complexation with binding species like biomolecules. The kinetic and thermodynamic parameters showed that the mechanism of crystal formation is moderately exothermic.

The binding energy of the SARS-CoV-2/Mpro-L<sub>TA</sub> complex and the calculated inhibition constant using docking simulation showed that the active L<sub>TA</sub> molecule has the ability to inhibit SARS-CoV-2.

© 2020 Elsevier B.V. All rights reserved.

## 1. Introduction

Coumarins (2H-chromen-2-ones) from natural sources are non-toxic and non-inhibitory against the biotransforming organism. These compounds have been identified in a large number of plants such as rutaceae, umbelliferae, legumes and orchids [1-3]. Many of the naturally and synthetic derivatives of coumarin have shown broad-spectrum of pharmacological, biological and physiological properties, including antibacterial, antifungal, antioxidant, anti-inflammatory, anti-allergic, antiviral, hepatoprotective, anti-tumor, anti-coagulant, anti-HIV and anti-carcinogenic agents [4-12]. Recently, this family of compounds has been used to prepare new drugs with very low toxicity [13,14], especially for skin and autoimmune diseases [15].

4-hydroxycoumarins are important precursors in the preparation of antifungal, bacteriostatic, anti-coagulant, potentially anti-HIV, spasmolytic drugs and herbicidal agents. This category of

products presents photochemical and photophysical characteristics and play a major role in modern optoelectronic [16-19].

Coumarins-fused pyridine hybrids are the most important type of pharmaceutical intermediates, and are defined in the literature as potential anti-osteoporotic agents [20]. They have a high biocompatibility due to the nitrogen atom that can form hydrogen bonds with biological molecules [21]. The complexes formed with coumarin-pyridine derivatives have attracted more attention from chemists because of their diverse structural design and scientific applications [22-24].

Since the listed positive effects of coumarin derivatives, we wondered if an alternative new synthetic molecule derived from coumarin might be designed to fight against infectious diseases caused by more virulent viruses. In perspective, this would prepare a drug against coronaviruses such as severe acute respiratory syndrome coronavirus 2 (SARS-CoV-2). The coronavirus disease 2019 (COVID-19) causes severe respiratory infection and is known to be very contagious [25]. Currently, there are no treatments available for SARS-CoV-2, therefore, treatment is focused on symptoms which may include dry cough, fever and pneumonia [26].

\* Corresponding author.

E-mail addresses: [achour\\_t@yahoo.fr](mailto:achour_t@yahoo.fr), [achour.terbouche@crapc.dz](mailto:achour.terbouche@crapc.dz) (A. Terbouche).

According to the work of Lima de Oliveira et al., the identification of small molecules (ligands) which specifically target the sensitive sites of viruses plays a very important role in antiviral drugs discovery [27]. Herein we wish to report on our preliminary studies towards this objective.

In this work, the new 4-[(pyridin-3-ylmethyl)amino]-2H-chromen-2-one ( $L_{TA}$ ) was synthesized and characterized by different techniques such as *single-crystal X-ray diffraction*, NMR, ATR, UV-Visible and cyclic voltammetry. Theoretical studies using DFT with B3LYP combined with the standard base set 6-31G+(d) were investigated to understand the chemical reactivity and the formation mechanism of  $L_{TA}$ . The aim of this study is also to evaluate the mode of interaction of  $L_{TA}$  with SARS-CoV-2/Main protease (Mpro), whose inhibition of this enzyme would prevent the virus from replication.

## 2. Materials and methods

### 2.1. Apparatus and reagents

Diffraction data were collected at 150 K on a D8 Venture Bruker AXS diffractometer equipped with a (CMOS) PHOTON 100 detector, Mo-K $\alpha$  radiation ( $\lambda = 0.71073 \text{ \AA}$ , multilayer monochromator). Crystallographic data for the structural analysis have been deposited at the Cambridge Crystallographic Data Center, CCDC No 1981639. These data can be obtained via <https://www.ccdc.cam.ac.uk>, e-mail: deposit\_reply@ccdc.cam.ac.uk.

The attenuated total reflectance (ATR) spectrum was carried out on a BRUKER LPHA-T Spectrometer. All nuclear magnetic resonance measurements ( $^1\text{H}$  NMR,  $^{13}\text{C}$  NMR and 2D-NMR) were performed at 25 °C with a Bruker Avance III Spectrometer.

The electronic spectra were recorded on a SECORD plus Spectrophotometer in the range 200–500 nm.

The electrochemical measurements were carried out using Potentiostat/Galvanostat Metrohm Autolab 302 N.

The theoretical calculations were performed using DFT/B3LYP/6-31G+(d) level of theory.

All reagents and solvents used to prepare the measurement solutions were of the highest purity and analytical grade from Sigma-Aldrich or Fluka chemicals Company.

### 2.2. Synthesis of ligand

The ligand (4-[(pyridin-3-ylmethyl)amino]-2H-chromen-2-one:  $L_{TA}$ ) was synthesized by adding 1.08 mL of 3-picollylamine (10 mmol) to 10 mmol (1.62 g) of 4-hydroxycoumarin dissolved in 10 mL of absolute ethanol. The mixture was stirred under reflux at 70 °C for 48 h.

The bright incolor crystals of the product were grown by slow evaporation technique in ethanol for two weeks.

The obtained crystals are soluble in acetone, ethanol, water, dichloromethane (DCM), chloroform ( $\text{CHCl}_3$ ) and dimethylsulfoxide (DMSO).

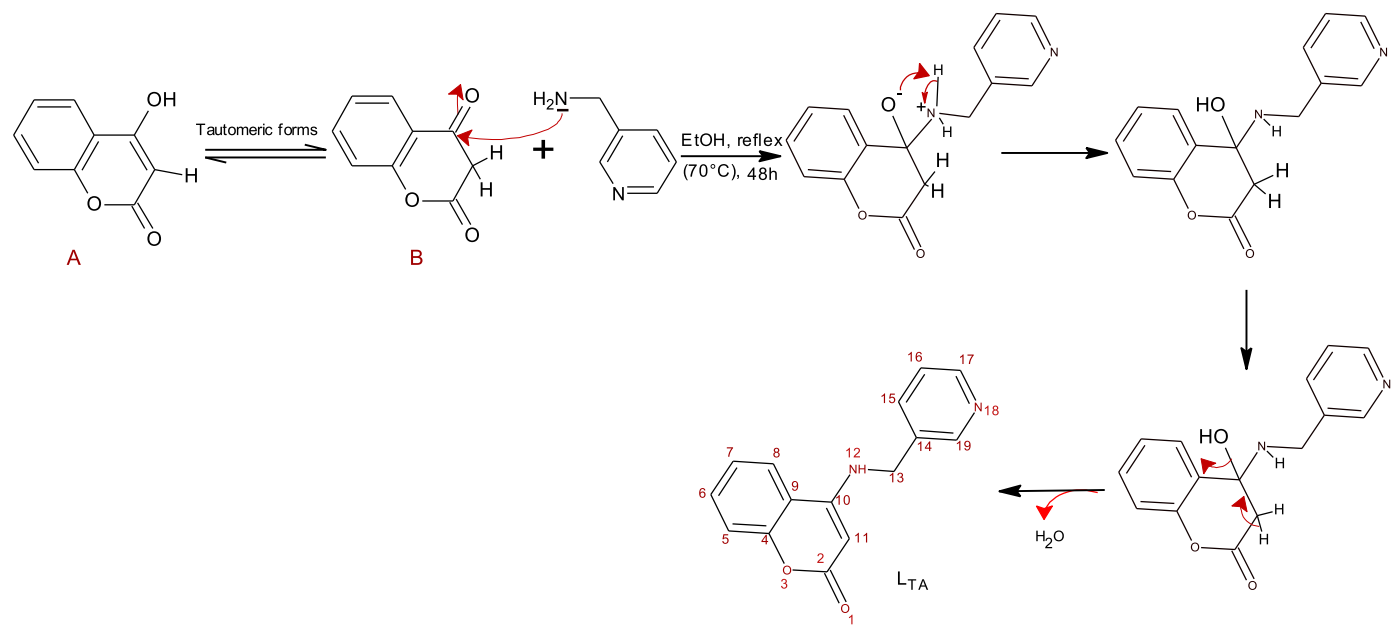
Yield: 56% (1.405 g); m.p 198 °C.  **$^1\text{H}$  NMR (400 MHz, DMSO, 25 °C, ppm,  $\delta$ ):** δ 4.59 (d,  $J = 5.9 \text{ Hz}$ , 2 H13,  $\text{CH}_2$ ); 5.17 (s, 1 H11, CH); 7.32 (dd,  $J = 8.3, 0.8 \text{ Hz}$ , 1 H5, CH); 7.36 (dd,  $J = 10.5, 3.4 \text{ Hz}$ , 1 H16, CH); 7.38–7.41 (m, 1 H8, CH); 7.58–7.64 (m, 1 H6, CH); 7.76–7.82 (m, 1 H15, CH); 8.12 (dd,  $J = 8.1, 1.1 \text{ Hz}$ , 1 H7, CH); 8.28–8.38 (m, 1 H12, NH); 8.49 (dd,  $J = 15.5, 4.2 \text{ Hz}$ , 1 H17, CH); 8.60–8.76 (m, 1 H19, CH).

**$^{13}\text{C}$  NMR (101 MHz, DMSO, 25 °C, ppm,  $\delta$ ):** 43.60 (C13); 83.14 (C11); 114.87 (C9); 117.44 (C5); 122.94 (C7); 123.91 (C16); 124.08 (C8); 132.48 (C6); 133.76 (C14); 135.40 (C15); 148.91 (C17); 149.23 (C19); 153.50 (C4); 153.58 (C10); 161.85 (C2).

**HSQC-NMR (101 MHz, DMSO, 25 °C, ppm,  $\delta$ ):** 4.59:43.60 (H13:C13); 5.17:83.14 (H11:C11); 7.32:117.44 (H5:C5); 7.36:123.91 (H16:C16); 7.38:124.08 (H8:C8); 7.58:132.48 (H6:C6); 7.76:135.40 (H15:C15); 8.12:122.94 (H7:C7); 8.49:148.91 (H17:C17); 8.60:149.23 (H19:C19).

**HMBC-NMR (101 MHz, DMSO, 25 °C, ppm,  $\delta$ ):** 4.59:133.76:135.40:148.91:153.58 (H13: C14:C15 :C17 :C10); 5.17:114.87:161.85 (H11:C9 :C2); 7.32:114.87:124.08:153.50 (H5:C9:C8 :C4); 7.36:133.76 (H16:C14); 7.38 :132.48:153.58 (H8 :C6 :C10); 7.58:122.94:153.50 (H6 :C7:C4); 7.76:148.91:149.23 (H15:C17:C19); 8.12:132.48:153.58 (H7:C6 :C10); 8.28:83.14:114.87 (H12:C11:C9); 8.60:133.76:148.91 (H19:C14:C17).

**Scheme 1** describes the synthesis mechanism of 4-[(pyridin-3-ylmethyl) amino]-2H-chromen-2-one. In solution, the likely tautomeric forms of 4-hydroxycoumarin are 2-hydroxy-4-chromenone (A) and 2, 4-chromandione (B) [28]. Indeed, synthesis of  $L_{TA}$  is carried out via nucleophilic attack of NH<sub>2</sub> group of



**Scheme 1.** Synthesis mechanism of ligand ( $L_{TA}$ ).

**Table 1**Crystal data and structure refinement for  $L_{TA}$ .

Empirical formula	$C_{15}H_{12}N_2O_2$
Formula weight (g/mol)	252.27
Temperature (K)	150
Wavelength (Å)	0.71073
Crystal system	Monoclinic
Space group	P 2 <sub>1</sub>
Unit cell dimensions	
a, b, c (Å)	$a = 11.9894(17)$ , $b = 7.3557(11)$ , $c = 14.733(2)$
$\alpha, \beta, \gamma$ (°)	$\alpha = 90$ , $\beta = 108.349(5)$ , $\gamma = 90$
Volume (Å <sup>3</sup> )	1233.3(3)
Z	4
Calculated density (g.cm <sup>-3</sup> )	1.359
Absorption coefficient $\mu$ (mm <sup>-1</sup> )	0.092
F(000)	528
Crystal size (mm)	0.290 × 0.210 × 0.080
Crystal color	colourless
Theta range for data collection (°)	2.639 to 27.557
$h_{min}, h_{max}$	-15.14
k <sub>min</sub> , k <sub>max</sub>	0.9
l <sub>min</sub> , l <sub>max</sub>	0.19
Reflections collected / unique	4244/4244
Reflections [ $I > 2\sigma(I)$ ]	3351
Completeness to theta <sub>max</sub>	0.981
Absorption correction type	multi-scan
Max. and min. transmission	0.993, 0.974
Refinement method	Full-matrix least-squares on F <sup>2</sup>
Data/restraints/parameters	4244/50/345
Goodness-of-fit on F <sup>2</sup>	1.346
Final R indices [ $I > 2\sigma(I)$ ]	$R_1 = 0.0858$ ; $wR_2 = 0.2233$
R indices (all data)	$R_1 = 0.1190$ ; $wR_2 = 0.2373$
$\Delta\rho$ (min, max) [e.Å <sup>-3</sup> ]	0.376; -0.381

3-picolyamine on the C10 carbonyl of 2, 4-chromandione with elimination of water molecule [29, 30], according to the following detailed mechanism:

### 3. Results and discussion

#### 3.1. Characterization of the ligand

##### 3.1.1. X-ray crystallography of $L_{TA}$

Well defined colourless crystals, crystal size =  $0.290 \times 0.210 \times 0.080$  mm has been selected and mounted on a cryoloop for X-ray diffraction analysis. The crystal data of  $L_{TA}$  ( $C_{15}H_{12}N_2O_2$ :  $M = 252.27$  g/mol) showed that the ligand crystallizes in monoclinic system with space group P2<sub>1</sub>. The crystallographic parameters are:  $Z = 4$ ,  $a = 11.9894(17)$  Å,  $b = 7.3557(11)$  Å,  $c = 14.733(2)$  Å,  $\alpha = 90^\circ$ ,  $\beta = 108.349(5)^\circ$ ,  $\gamma = 90^\circ$ ,  $V = 1233.3(3)$  Å<sup>3</sup>,  $\mu(\text{Mo-K}\alpha) = 0.092$  mm<sup>-1</sup> and  $D_c = 1.359$  g.cm<sup>-3</sup>. A total of 4244 reflections were collected. Final  $R_1 = 0.0858$  [ $I > 2\sigma(I)$ ] and  $wR_2 = 0.2373$  (all data). Data completeness to theta 27.557° = 98.1%.

ORTEP representation of the product is shown in Fig. 1a. All non-hydrogen atoms were refined with anisotropic displacement parameters.

There are two asymmetric-independent molecules of  $L_{TA}$  in the unit cell with a slight difference in the bond lengths and angles. The main difference between the two molecules arises primarily from 3-picolyamine group about the torsion angles N(12)-C(13)-C(14)-C(15) of structure 1 (-62.4°) and N(32)-C(33)-C(34)-C(35) of structure 2 (28.1°).

The crystal data, the conditions of data collection, isotropic and anisotropic displacement parameters, bond lengths (Å), bond angles (°) and torsion angles (°) are summarized in Table 1, 2 and Tables S1, S2. There are three inequivalent hydrogen bonds in the crystal (Fig. 1b and Table S3). The first and the second hydrogen

bonds (N12-H12•••O21 and N32-H32•••O1) are short, their hydrogen bond distance are H12•••O21 = 1.99 Å and H32•••O1 = 1.97 Å, respectively.

The third hydrogen bond, C39-H39•••N18 (not shown in Fig. 1b) should be weaker because it corresponds a large distance H39•••N18 = 2.61 Å.

#### 3.1.2. Geometry optimization of ligand

In order to obtain stable structure, an optimization of the geometrical parameters of ligand  $L_{TA}$  has been carried out at DFT levels of theory [31] using the Becke's three parameter hybrid exchange functional in combination with Lee-Yang-Parr correlation functional (B3LYP) [32] at 6-31+G(d) basis sets. All calculations were obtained with the Gaussian09 program package [33].

The optimized parameters, namely, bond lengths and angles and Dihedral angles calculated by B3LYP/6-31+G(d,) and found by XRD are reported in Table 2, according to the numbering atoms given in Scheme 1 and Fig. 2. Table 2a, Table 2b, Table 2c.

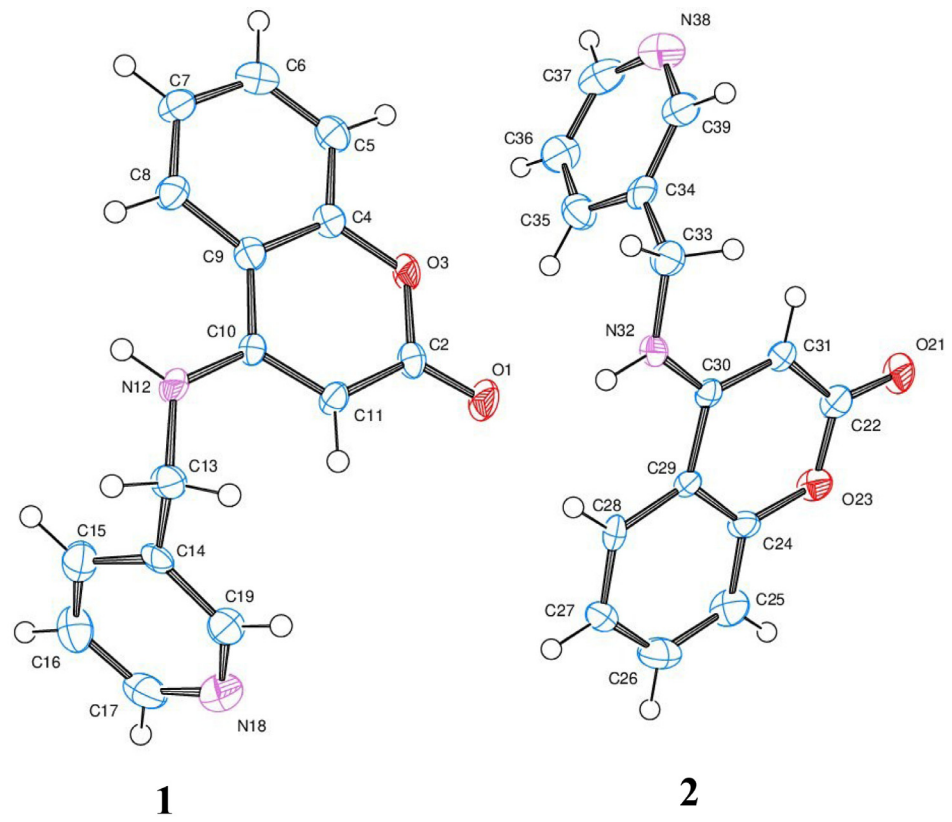
The quantitative-chemical calculations of the two systems ( $L_{TA(C1-C19)}$ ) and ( $L_{TA(C21-C39)}$ ) performed theoretically give similar results for bond lengths and angles, which are in agreement with the X-ray diffraction data. The slight differences found between the experimentally and theoretically calculated dihedral angles are due to the molecular interactions not taken into account by this chosen theoretical method, and to the effects of the solvent which have been neglected (gas phase).

However, the analysis of the total energy shows the same energy for:

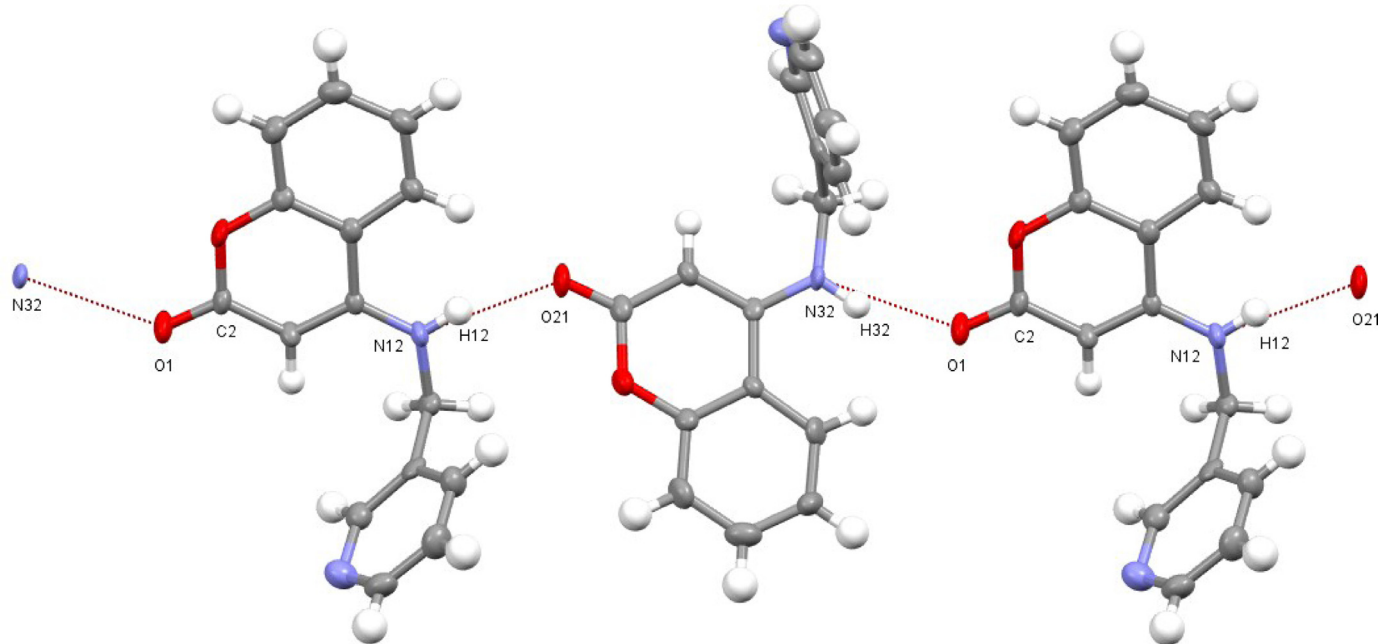
$L_{TA(C1-C19)}$  (-838.80986151 a.u) and  $L_{TA(C21-C39)}$  (-838.80986137 a.u) with a slight difference of around  $10^{-7}$ . For this,  $L_{TA(C1-C19)}$  structure was chosen for the rest of the theoretical study.

**Table 2a**Bond lengths (Å) obtained by XRD and DFT/B3LYP/6-31 + G(d) for the ligand  $L_{TA}$ .

Atoms Structure 1	DRX	DFT	Atoms Structure 2	DRX	DFT
O1 - C2	1.223(10)	1.2129	O21 - C22	1.218(10)	1.2129
C2 - O3	1.373(10)	1.4041	C22 - O23	1.384(11)	1.4040
C2 - C11	1.427(11)	1.4409	C22 - C31	1.419(11)	1.4409
O3 - C4	1.367(10)	1.3603	O23 - C24	1.373(10)	1.3603
C4 - C5	1.398(11)	1.3998	C24 - C29	1.396(11)	1.4089
C4 - C9	1.409(11)	1.4089	C24 - C25	1.397(12)	1.3998
C5 - C6	1.375(13)	1.3896	C25 - C26	1.383(13)	1.3896
C5 - H5	0.9500	1.0854	C25 - H25	0.9500	1.0854
C6 - C7	1.395(13)	1.4028	C26 - C27	1.379(13)	1.4028
C6 - H6	0.9500	1.0865	C26 - H26	0.9500	1.0865
C7 - C8	1.381(12)	1.3899	C27 - C28	1.376(12)	1.3899
C7 - H7	0.9500	1.0860	C27 - H27	0.9500	1.0860
C8 - C9	1.412(11)	1.4094	C28 - C29	1.417(11)	1.4094
C8 - H8	0.9500	1.0868	C28 - H28	0.9500	1.0868
C9 - C10	1.465(11)	1.4658	C29 - C30	1.468(11)	1.4658
C10 - N12	1.344(10)	1.3712	C30 - N32	1.336(10)	1.3712
C10 - C11	1.366(11)	1.3729	C30 - C31	1.376(11)	1.3728
C11 - H11	0.9500	1.0820	C31 - H31	0.9500	1.0820
N12 - C13	1.457(11)	1.4563	N32 - C33	1.451(11)	1.4563
N12 - H12	0.8800	1.0078	N32 - H32	0.8800	1.0077
C13 - C14	1.516(12)	1.5222	C33 - C34	1.524(12)	1.5222
C13 - H13A	0.9900	1.0964	C33 - H33A	0.9900	1.0964
C13 - H13B	0.9900	1.0996	C33 - H33B	0.9900	1.0996
C14 - C19	1.381(12)	1.4012	C34 - C35	1.382(13)	1.3972
C14 - C15	1.388(13)	1.3972	C34 - C39	1.384(12)	1.4013
C15 - C16	1.382(14)	1.3948	C35 - C36	1.372(14)	1.3948
C15 - H15	0.9500	1.0868	C35 - H35	0.9500	1.0868
C16 - C17	1.371(14)	1.3970	C36 - C37	1.367(14)	1.3970
C16 - H16	0.9500	1.0864	C36 - H36	0.9500	1.0864
C17 - N18	1.347(15)	1.3395	C37 - N38	1.355(16)	1.3395
C17 - H17	0.9500	1.0882	C37 - H37	0.9500	1.0882
N18 - C19	1.347(13)	1.3379	N38 - C39	1.356(14)	1.3379



(a)



(b)

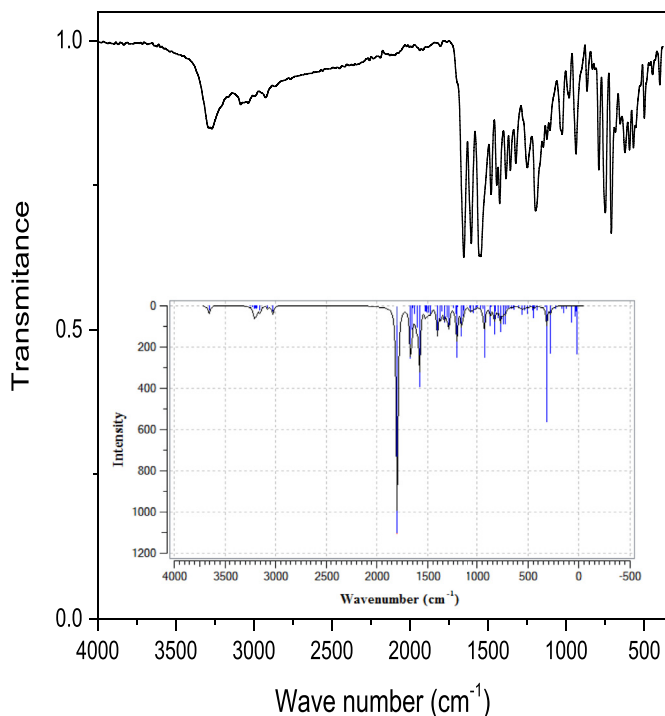
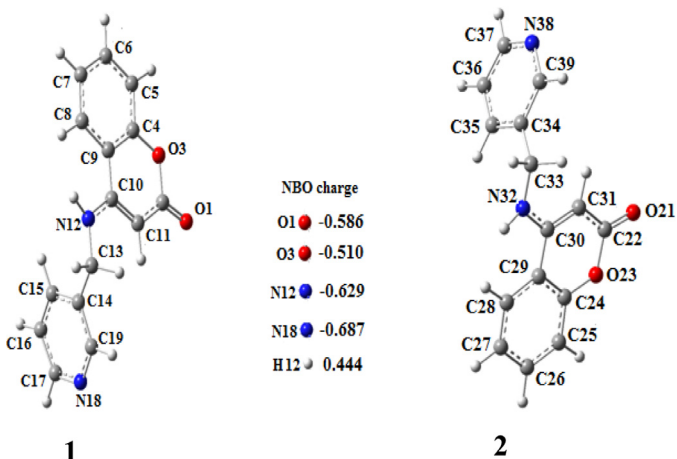
**Fig. 1.** Structure of ligand: (a) ORTEP and (b) hydrogen bonds representation.

**Table 2b**  
Bond angles ( $^{\circ}$ ) obtained by XRD and DFT/B3LYP/6-31 + G(d) for the ligand L<sub>TA</sub>.

Atoms Structure 1	DRX	DFT	Atoms Structure 2	DRX	DFT
O1 - C2 - O3	115.9(8)	116.88	O21 - C22 - O23	116.1(8)	116.88
O1 - C2 - C11	125.3(8)	126.61	O21 - C22 - C31	126.3(9)	126.62
O3 - C2 - C11	118.8(8)	116.50	O23 - C22 - C31	117.6(8)	116.50
C4 - O3 - C2	120.6(6)	122.06	C24 - O23 - C22	121.6(7)	122.06
O3 - C4 - C5	115.6(8)	116.28	O23 - C24 - C29	122.1(7)	122.46
O3 - C4 - C9	122.2(7)	122.46	O23 - C24 - C25	116.1(8)	116.28
C5 - C4 - C9	122.3(8)	121.26	C29 - C24 - C25	121.8(8)	121.26
C6 - C5 - C4	119.1(9)	119.67	C26 - C25 - C24	119.2(9)	120.20
C5 - C6 - C7	120.2(9)	120.20	C27 - C26 - C25	120.1(9)	119.80
C8 - C7 - C6	120.9(9)	119.80	C28 - C27 - C26	121.0(9)	119.80
C7 - C8 - C9	120.7(9)	121.28	C27 - C28 - C29	120.6(8)	121.28
C4 - C9 - C8	116.9(8)	117.78	C24 - C29 - C28	117.3(7)	117.78
C4 - C9 - C10	118.3(8)	117.30	C24 - C29 - C30	117.6(7)	117.30
C8 - C9 - C10	124.8(8)	124.92	C28 - C29 - C30	125.1(8)	124.92
N12 - C10 - C11	123.8(8)	122.70	N32 - C30 - C31	124.1(8)	122.69
N12 - C10 - C9	119.1(8)	118.58	N32 - C30 - C29	117.9(7)	118.58
C11 - C10 - C9	117.1(7)	118.72	C31 - C30 - C29	118.1(8)	118.72
C10 - C11 - C2	123.1(8)	122.93	C30 - C31 - C22	123.0(8)	122.93
C10 - N12 - C13	123.9(8)	123.84	C30 - N32 - C33	123.5(8)	123.84
C10 - N12 - H12	118.1	116.77	C30 - N32 - H32	118.3	116.76
C13 - N12 - H12	118.1	115.91	C33 - N32 - H32	118.3	115.91
N12 - C13 - C14	114.3(8)	114.81	N32 - C33 - C34	113.5(9)	114.81
C19 - C14 - C15	118.0(9)	117.39	C35 - C34 - C39	117.4(9)	117.39
C19 - C14 - C13	120.2(9)	119.76	C35 - C34 - C33	122.3(9)	122.81
C15 - C14 - C13	121.7(8)	122.81	C39 - C34 - C33	120.3(9)	119.76
C16 - C15 - C14	119.0(9)	119.054	C36 - C35 - C34	120.3(9)	119.05
C17 - C16 - C15	118.7(11)	118.67	C37 - C36 - C35	118.6(11)	118.68
C17 - C16 - H16	120.7	120.32	C37 - C36 - H36	120.7	120.32
C15 - C16 - H16	120.7	121.00	C35 - C36 - H36	120.7	121.00
N18 - C17 - C16	124.0(10)	123.21	N38 - C37 - C36	123.7(11)	123.21
C16 - C17 - H17	117.9	120.70	C37 - N38 - C39	116.2(10)	117.35
C17 - N18 - C19	116.0(9)	117.35	N38 - C39 - C34	123.8(10)	124.32

**Table 2c**  
Torsion angles ( $^{\circ}$ ) obtained by XRD and DFT/B3LYP/6-31 + G(d) for the ligand L<sub>TA</sub>.

Atoms Structure 1	DRX	DFT	Atoms Structure 2	DRX	DFT
O1-C2-O3-C4	-179.2(10)	179.30	O21-C22-O23-C24	-179.4(10)	-179.30
C11-C2-O3-C4	0.1(14)	-1.16	C22-O23-C24-C29	0.6(15)	-0.85
C2-O3-C4-C5	179.6(10)	-179.10	C22-O23-C24-C25	179.9(10)	179.09
C2-O3-C4-C9	-0.7(14)	0.84	O23-C24-C25-C26	179.3(11)	-179.51
O3-C4-C5-C6	179.0(10)	179.51	C24-C25-C26-C27	0.8(19)	0.15
C9-C4-C5-C6	-0.7(16)	-0.42	C26-C27-C28-C29	1.3(18)	-0.12
C4-C5-C6-C7	1.5(17)	-0.15	O23-C24-C29-C28	-178.9(10)	179.12
C6-C7-C8-C9	-0.3(18)	0.11	C25-C24-C29-C28	1.8(15)	-0.82
O3-C4-C9-C8	179.8(10)	-179.12	O23-C24-C29-C30	-0.8(14)	-0.64
C5-C4-C9-C8	-0.5(15)	0.81	C25-C24-C29-C30	179.9(10)	179.43
O3-C4-C9-C10	0.6(14)	0.64	C27-C28-C29-C30	-179.6(10)	-179.60
C5-C4-C9-C10	-179.7(10)	-179.43	C24-C29-C30-N32	-178.9(9)	-179.20
C7-C8-C9-C10	-179.9(10)	179.60	C28-C29-C30-N32	-1.0(14)	1.06
C4-C9-C10-N12	-179.7(9)	179.20	C24-C29-C30-C31	1.3(13)	1.75
C8-C9-C10-N12	1.2(16)	-1.05	C28-C29-C30-C31	179.2(10)	-177.99
C4-C9-C10-C11	0.1(14)	-1.75	N32-C30-C31-C22	178.6(10)	179.52
C8-C9-C10-C11	-179.1(10)	178.00	C29-C30-C31-C22	-1.5(15)	-1.47
N12-C10-C11 - C2	179.1(11)	-179.53	O21-C22-C3-C30	179.8(11)	-179.46
C9-C10-C11-C2	-0.7(15)	1.46	C31-C30-N32-C33	-1.0(15)	-8.97
O1-C2-C11-C10	179.9(12)	179.47	C29-C30-N32-C33	179.2(9)	172.02
O3-C2-C11-C10	0.6(16)	-0.03	C30-N32-C33-C34	77.7(12)	79.70
C11-C10-N12-C13	3.3(16)	8.97	N32-C33-C34-C35	28.1(13)	26.10
C9-C10-N12-C13	-176.9(9)	-172.02	N32-C33-C34-C39	-154.1(9)	-156.21
C10-N12-C13-C14	-79.0(12)	-79.69	C39-C34-C35-C36	2.3(16)	-0.36
N12-C13-C14-C19	118.2(10)	156.24	C33-C34-C35-C36	-179.8(10)	177.38
N12-C13-C14-C15	-62.4(12)	-26.07	C34-C35-C36-C37	-1.0(18)	-0.26
C19-C14-C15-C16	-0.2(15)	0.36	C35-C36-C37-N38	-1.0(2)	0.52
C13-C14-C15-C16	-179.6(10)	-177.38	C36-C37-N38-C39	1.0(2)	-0.10
C14-C15-C16-C17	-0.3(17)	0.26	C37-N38-C39-C34	0.5(18)	-0.60
C15-C16-C17-N18	0.3(19)	-0.52	C35-C34-C39-N38	-2.1(16)	0.84
C16-C17-N18-C19	0.2(17)	0.09	C33-C34-C39-N38	179.9(10)	-176.98
C17-N18-C19-C14	-0.8(16)	0.60			
C15-C14-C19-N18	0.8(15)	-0.83			
C13-C14-C19-N18	-179.8(10)	176.98			



### 3.1.3. Spectroscopy and spectrophotometry studies

The ATR spectrum was recorded to investigate the vibration modes of the functional groups and thus provide information on the structural dynamics of the ligand. In this study, the experimental spectrum of  $L_{TA}$  was superposed on that obtained theoretically (Fig. 3). The assignments of the various stretching and bending vibrations of the ligand were shown in Table S4.

The functional groups present in  $L_{TA}$  correspond to the frequencies at which absorption are located. The characteristic vibration frequencies for the studied compound are given as follows:

In the experimental spectrum of  $L_{TA}$ , N-H stretching vibration band is observed at  $3286\text{ cm}^{-1}$  and its deformation vibration band is located at  $1574\text{ cm}^{-1}$ . However, the theoretical spectrum showed N-H stretching and deformation vibrations at  $3282\text{ cm}^{-1}$  and  $1578\text{ cm}^{-1}$ , respectively.

**Table 3**

Results of second-order perturbation calculations of the Fock matrix on a NBO basis corresponding to the intramolecular interaction of ligand  $L_{TA}$ .

Donor (i)	Type	Acceptor (j)	Type	$E(2)$	$(\xi_j - \xi_i)$	$(F_{i,j})$
$C_{17} - C_{16}$	$\pi$	$C_{15} - C_{14}$	$\pi^*$	22.28	0.28	0.071
	$\pi$	$C_{19} - N_{18}$	$\pi^*$	18.16	0.26	0.062
$C_{15} - C_{14}$	$\pi$	$C_{17} - C_{16}$	$\pi^*$	17.50	0.28	0.064
	$\pi$	$C_{19} - N_{18}$	$\pi^*$	27.14	0.27	0.076
$C_{19} - N_{18}$	$\pi$	$C_{17} - C_{16}$	$\pi^*$	25.39	0.32	0.081
	$\pi$	$C_{15} - C_{14}$	$\pi^*$	13.80	0.32	0.060
$C_7 - C_8$	$\pi$	$C_9 - C_4$	$\pi^*$	16.85	0.28	0.063
	$\pi$	$C_5 - C_6$	$\pi^*$	19.63	0.29	0.067
$C_9 - C_4$	$\pi$	$C_7 - C_8$	$\pi^*$	20.47	0.29	0.070
	$\pi$	$C_5 - C_6$	$\pi^*$	15.74	0.29	0.062
	$\pi$	$C_{10} - C_{11}$	$\pi^*$	17.49	0.29	0.065
$C_5 - C_6$	$\pi$	$C_7 - C_8$	$\pi^*$	18.29	0.28	0.064
	$\pi$	$C_9 - C_4$	$\pi^*$	22.29	0.27	0.072
$C_{10} - C_{11}$	$\pi$	$C_2 - O_1$	$\pi^*$	27.15	0.30	0.082
LP (1) $N_{18}$	-	$C_{14} - C_{19}$	$\pi^*$	10.09	0.90	0.086
LP (1) $N_{12}$	-	$C_{10} - C_{11}$	$\pi^*$	45.86	0.30	0.106
LP (2) $O_1$	-	$C_2 - C_{11}$	$\pi^*$	16.22	0.72	0.100
	-	$C_2 - O_3$	$\pi^*$	40.29	0.55	0.134
	-	$C_9 - C_4$	$\pi^*$	32.64	0.34	0.098
-	-	$C_2 - O_1$	$\pi^*$	34.06	0.35	0.099

$E(2)$ : Stabilization (delocalization) energy (kJ/mol).

$(\xi_j - \xi_i)$ : Energy difference (a.u) between donor (i) an acceptor (j) NBO orbitals.

$(F_{i,j})$ : Fock matrix elements (a.u) between i and j NBO orbitals.

**Table 4**

Calculated energy gap  $|\Delta E|$  and global reactive descriptors (eV) for  $L_{TA}$  using B3LYP/6-31+G(d).

Reactivity descriptors	Formula	$L_{TA}$
$ \Delta E $	$ E_{LUMO} - E_{HOMO} $	4.685
Electronic ionization ( $I$ )	$I = -E_{HOMO}$	6.541
Electronic affinity ( $A$ )	$A = -E_{LUMO}$	1.856
Electronegativity ( $\chi$ )	$\chi = -[E_{LUMO} + E_{HOMO}] / 2$	4.199
Chemical potential ( $\mu$ )	$\mu = [E_{LUMO} + E_{HOMO}] / 2$	-4.199
Chemical hardness ( $\eta$ )	$\eta = [E_{LUMO} - E_{HOMO}]$	4.685
Global softness ( $S$ ) (eV) $^{-1}$	$S = 1/\eta$	0.214
Electrophilicity index ( $\omega$ )	$\omega = \mu^2 / 2\eta$	1.881
Nucléophilie index ( $N$ )	$N = E_{HOMO} - E_{HOMO(TCE)}$	2.868

TCE : Tetra Cyano Ethylene.

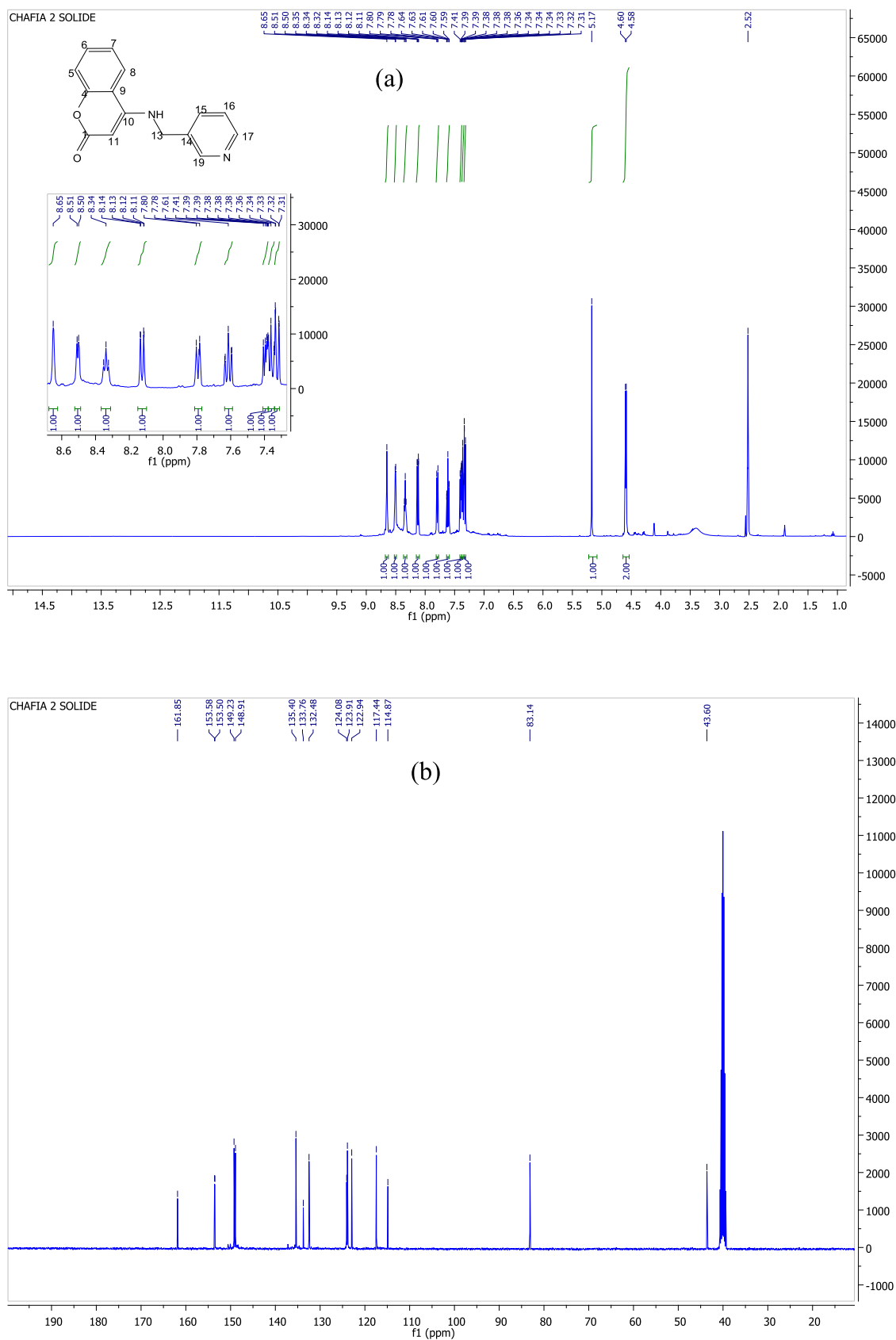
The symmetric and asymmetric C–H stretching vibrations of  $CH_2$  group can be found between 2850 and 3050  $\text{cm}^{-1}$  [34, 35]. For this ligand, C–H stretching vibrations are observed theoretically and experimentally in the range 2900–3050  $\text{cm}^{-1}$ , and the deformation bands are found around 1468  $\text{cm}^{-1}$  in both theoretically and experimental spectra. The other bands of C–H at 770–997  $\text{cm}^{-1}$  are assigned to the out-of-plane deformation vibrations.

C–N stretching vibrations are located at 1350  $\text{cm}^{-1}$ , whereas these calculated with B3LYP program are given at 1335  $\text{cm}^{-1}$ .

In the ATR spectrum, C=O stretching modes are observed at 1672  $\text{cm}^{-1}$  associated theoretically to the peak appeared at 1760  $\text{cm}^{-1}$  [36]. However, the peaks found in the range 1270–1300  $\text{cm}^{-1}$  and at 711  $\text{cm}^{-1}$  are assigned to the stretching and deformation vibrations of the C–O groups, respectively.

NMR spectroscopy is one of the most powerful instruments for organic and inorganic structural identifications. The chemical shift displacements were calculated by the GIAO model (Gauge Including Atomic Orbital) [37, 38] in DMSO using the PCM model.

$^1\text{H}$  NMR and  $^{13}\text{C}$  NMR spectra of the ligand were recorded in deuterated DMSO solution and were reported in Fig. 4a, b. HSQC–NMR and HMBC–NMR spectra are shown in Figs. S1a, b.

**Fig. 4.** NMR spectra of ligand: (a)  $^1\text{H}$  NMR and (b)  $^{13}\text{C}$  NMR.

**Table 5**

Kinetic and computed thermodynamic parameters at temperature of 298.15 K of  $L_{TA}$  formation reaction.

Parameters	Values
$\Delta H^\circ$ (kcal. mol <sup>-1</sup> )	-18.4563241
$\Delta G^\circ$ (kcal. mol <sup>-1</sup> )	-18.7914145
$\Delta S^\circ$ (kcal. mol <sup>-1</sup> )	0.0011255
$\Delta G^*$ (kcal. mol <sup>-1</sup> )	59.5896046
Total energy (Hartree)	-915.2642448
Zero-point vibrational energy (kcal. mol <sup>-1</sup> )	166.32076
Zero-point correction*	0.265049
Thermal correction to energy*	0.284376
Thermal correction to enthalpy*	0.285320
Thermal correction to Gibbs free energy*	0.211424
Sum of electronic and zero-point energies*	-914.999196
Sum of electronic and thermal energies*	-914.979869
Sum of electronic and thermal enthalpies*	-914.978925
Sum of electronic and thermal free energies*	-915.052821
Entropy, S (kcal.mol <sup>-1</sup> )	0.155528

\* in Hartree/particle.

The theoretical and experimental chemical shifts in proton and carbon NMR of  $L_{TA}$  molecule noted  $\delta_{Cal}$  and  $\delta_{Exp}$ , respectively, are shown in Table S5.

The chemical shift between 8.28 and 8.38 ppm in the experimental proton NMR spectrum is attributed to H12 proton bound to N12 nitrogen. The same proton presents a chemical shift of 4.83 ppm in the theoretical spectrum. The atomic charge on H12 is found to be large positive (Fig. 2) as electronegative N atom is attached with this hydrogen. Therefore, H12 is observed on higher ppm scale [39].

The proton signals on the aromatic ring are observed in the region 7.32–8.12 ppm and at 7.11–7.51 ppm in the experimental and theoretical spectrum, respectively. The protons on pyridine ring are seen experimentally between 7.36 and 8.76 ppm and theoretically between 7.14 and 8.49 ppm.

The junction between the cycles shows proton resonances between 4.58–4.60 ppm in the experimental spectrum and between 4.49–4.37 ppm in the theoretical spectrum.

Correlation between experimental and calculated chemical shifts of <sup>1</sup>H NMR and <sup>13</sup>C-NMR are given in Figs. S1 c, d. <sup>13</sup>C NMR calibration plot showed a good linear relationship between the experimental and theoretical chemical shifts, with correlation coefficient  $R^2=0.998$ .

The lower correlation coefficient ( $R^2=0.80$ ) obtained from <sup>1</sup>H NMR calibration plot is due to the chemical shift of the proton at position 12 found experimentally in the range 8.28–8.38 ppm and theoretically at 4.83 ppm.

In summary, the values of the experimental and theoretical chemical shift displacements of <sup>1</sup>H and <sup>13</sup>C of the ligand are in agreement.

The chemical shift of all protons and carbon resonances have also been obtained based on 2D-NMR experiment.

In Heteronuclear Single Quantum Coherence (HSQC) experiment (Fig. S1a), the appearing cross-peaks correlation indicate the assignment of all protonated carbon atoms: 4.59:43.60 (H13:C13); 5.17:83.14 (H11:C11); 7.32:117.44 (H5:C5); 7.36:123.91 (H16:C16); 7.38:124.08 (H8:C8); 7.58:132.48 (H6:C6); 7.76:135.40 (H15:C15); 8.12:122.94 (H7:C7); 8.49:148.91 (H17:C17); 8.60:149.23 (H19:C19).

According to the Heteronuclear Multiple Bond Correlation (HMBC) NMR spectrum (Fig. S1b), the cross-peaks correlation provided the coupling between protons and neighboring carbons, so quaternary carbon atoms have been precisely located:

4.59:133.76:135.40:148.91:153.58 (H13:C14:C15:C17:C10); 5.17:114.87:161.85 (H11:C9 :C2); 7.32:114.87:124.08:153.50 (H5:C9:C8:C4); 7.36:133.76 (H16:C14); 7.38 :132.48:153.58 (H8 :C6 :C10); 7.58:122.94:153.50 (H6:C7:C4); 7.76:148.91:149.23

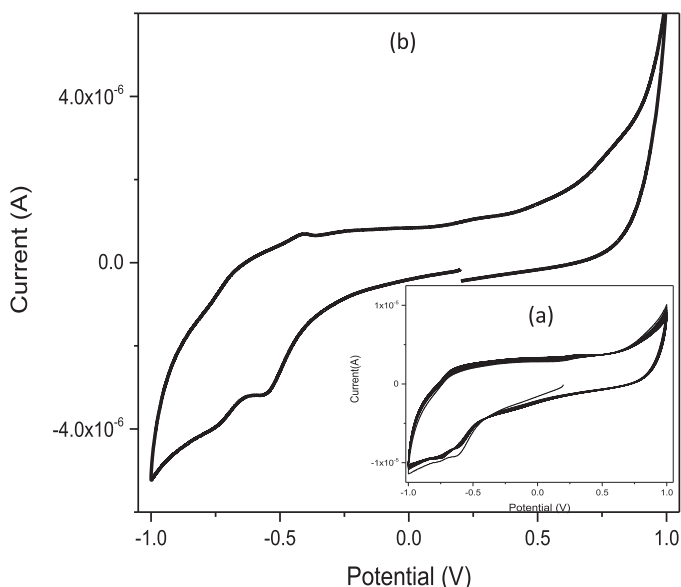


**Fig. 5.** (a) Cyclic voltammograms (25 cycles) and (b) Cyclic voltammetry of ligand in DMSO and tetrabutylammonium hexafluorophosphate (TBAPF<sub>6</sub>: 0.1 M), scan rate: 20 mV/s.

(H15:C17:C19); 8.12:132.48:153.58 (H7:C6:C10); 8.28:83.14:114.87 (H12:C11:C9); 8.60:133.76:148.91 (H19:C14:C17).

In the electron spectrum recorded in the range 200–500 nm in ethanol (Fig. S2), two peaks are observed at 210 nm and 297 nm which are attributed to  $\pi\rightarrow\pi^*$  and  $n\rightarrow\pi^*$  transitions of C = C and C = O groups, respectively.

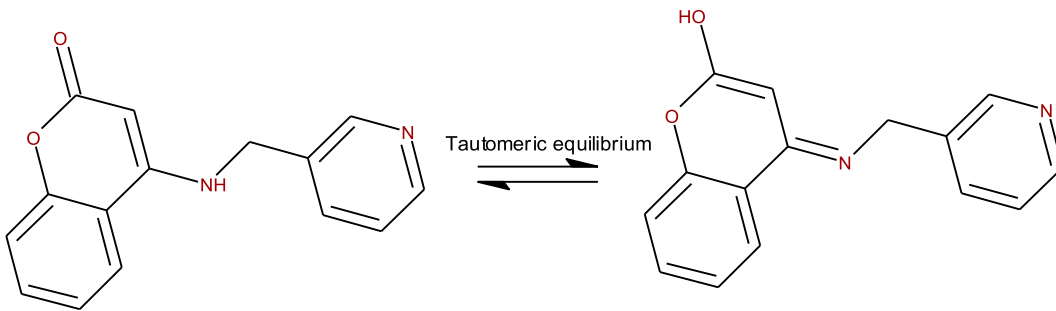
The TD-DFT method [40, 41] is a reliable approach widely used to predict the spectra of electronic absorptions. The theoretical prediction of the electron absorption spectrum of  $L_{TA}$  was realized using the TD-DFT/B3LYP/6-31+G (d) method on optimized geometries. The calculations were carried out in ethanol solvent with PCM calculation. The calculated excitation energies, oscillator forces (f) and wavelengths ( $\lambda$ ) are given in Table S6. The estimated UV-visible spectrum of  $L_{TA}$  is presented in Fig. S2. The strongest electronic absorption observed at 294 nm is due to HOMO-1  $\rightarrow$  LUMO (5.61%) and HOMO  $\rightarrow$  LUMO (89.13%) transitions with an oscillator strength  $f = 0.14$  and electronic transition energy  $\Delta E = 4.22$  eV.

### 3.2. Stability and electrochemical behavior of ligand $L_{TA}$

The electrochemical behavior of the ligand was studied by cyclic voltammetry in DMSO and tetrabutylammonium hexafluorophosphate (TBAPF<sub>6</sub>) at a potential scan rate of 20 mV.s<sup>-1</sup>. Platinum, glassy carbon and saturated Ag/AgCl were used as working electrode, a counter electrode and a reference electrode of platinum, respectively.

To assess the stability of the ligand, CVs were recorded up to 25 cycles at scanning rate of 20 mV/s (Fig. 5a). The results obtained showed good reproducibility of the voltammograms, indicating the stability of this product ( $L_{TA}$ ) at room temperature.

The recorded voltammogram of the ligand (Fig. 5b) gives a cathodic peak at  $E_{pc}=-0.56$  V assigned to the reduction of C = O to OH group which in turn oxidizes at  $E_{pa}=-0.41$  V. In the anodic part, the second peak at  $E_{pa}=0.30$  V is due to the oxidation of N-H to imine group (C = N) [42]. This result reveals the presence of two tautomeric forms of the ligand in solution (Scheme 2).

**Scheme 2.** Tautomeric equilibrium of ligand ( $L_{TA}$ ).

### 3.3. Chemical reactivity

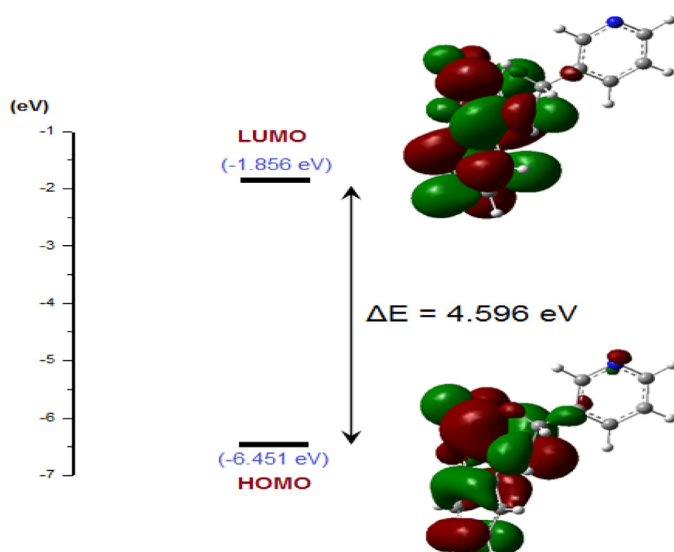
#### 3.3.1. Orbital analysis

Functional density theory (DFT) in computational chemistry is a highly dynamic tool used in several research projects to predict and determine structural properties, chemoselectivity, stereoselectivity, regioselectivity, reaction mechanisms, energy profiles and various spectroscopic characterizations.

Molecular orbitals represented by the Highest Occupied Molecular Orbital (HOMO) and Lowest Unoccupied Molecular Orbital (LUMO) are important quantum chemistry parameters. Indeed, the knowledge of the frontier orbitals allows determining the molecular properties [43].

The difference in energy between LUMO and HOMO, corresponding to energy gap ( $\Delta E$ ), serves to characterize the chemical reactivity and the kinetic stability of the molecule. The highest occupied molecular orbitals and lowest unoccupied molecular orbitals of the ligand have been studied and the results were given in Fig. 6. The HOMO density plot of the stable ligand showed that the electron density is observed essentially on the 4-amino-2H-chromen-2-one ring and on the nitrogen of the pyridine ring, whereas the LUMO showed the localization of electron density just on the 4-amino-2H-chromen-2-one ring. This result predicts the localization of the electrophilic and nucleophilic attack sites of  $L_{TA}$ .

On the other hand, we also note that the value of the energy gap of this ligand is significant (4.596 eV), this indicates that  $L_{TA}$  is more stable due to its hard character. This result was confirmed by the analysis of the global reactivity indices (Section 3.3.5).

**Fig. 6.** Gap energy and Frontier molecular orbitals (HOMO and LUMO) of  $L_{TA}$ .

#### 3.3.2. Molecular electrostatic potential (MEP)

MEP is a very useful method to investigate the electrophilic and nucleophilic attack sites. It is directly related to the electron density, as well as hydrogen bonding interactions [44, 45]. Molecular electrostatic potential was evaluated using the B3LYP/6-31+G(d) method. According to Fig. 7a, we observe different regions: those colored in red and yellow correspond to electron-rich sites (maximum negative potential), the blue region due to electron-poor sites and the green regions correspond to neutral sites (region of zero potential).

For  $L_{TA}$ , the most negative regions (red and yellow) cover the carbonyl group of coumarin and the intracyclic nitrogen of 3-picolyamine. The high electronegativity of these groups (C = O and N) presents the most reactive part (the most suitable sites for electrophilic attack) of the ligand. Whereas, the blue region represents the site of highest reactivity to nucleophilic attacks.

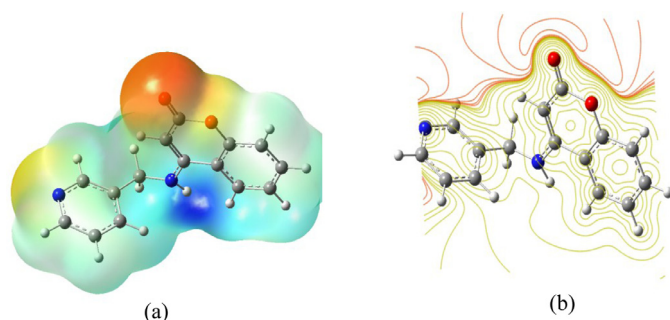
In addition, the contour MEP is a two-dimensional (2D) representation of the areas where the relative electron density values are within a specific margin at 0010. For our compound, the contoured MEP for the positive and negative potentials is given in Fig. 7b.

The found results allow giving information about the sites of intermolecular attacks (electrophilic and nucleophilic attacks) and the MEP map.

#### 3.3.3. Natural bond order analysis (NBO)

The atomic charges play an important role in the application of quantum chemical calculations to molecular systems [46] because they affect dipole moment, molecular polarizability and electronic structure [43]. Atomic charges can be used to describe the processes of electronegativity equalization and predicting the charge transfer in chemical reactions [47, 48]. The distribution of the net charges on the main  $L_{TA}$  atoms and the calculations were made using NBO theory.

The electrostatic charge values of the ligand obtained at DFT/B3LYP/6-31+G(d) show that O1(-0.586), O3(-0.510),

**Fig. 7.** (a) MEP surface and (b) MEP contour [density lie within a specific range at (0010)] of  $L_{TA}$ .

N12(−0.629) and N18(−0.687) are electron-rich sites (net negative charges), while H12(0.444) is electron-poor site (net positive charges). According to this result, we conclude that the O1, O3, N12 and N18 sites are more favored for electrophilic attacks, but the H12 site is more favored for nucleophilic attacks. This result is in agreement with that found using molecular electrostatic potential (MEP).

### 3.3.4. Analysis of stabilization energies E(2)

The Natural Bond Orbital (NBO) method provides information on the intramolecular and intermolecular interactions that can form within the molecule. Indeed, NBO determines the stabilization energies of a given compound using second-order perturbation theory [37]. For each donor NBO (*i*) and acceptor NBO (*j*), the stabilization energy *E*(2) associated with electron delocalization between donor and acceptor is determined as follows [49, 50]:

$$E(2) = \Delta E_{ij} = q_i \frac{F(i,j)^2}{\xi_j - \xi_i}$$

With *E*(2) is the stabilization (delocalization) energy (kJ/mol), ( $\xi_j - \xi_i$ ) is the difference in energy (a.u) between the donor (*i*) and acceptor (*j*) NBO orbitals, ( $F_{i,j}$ ) is the Fock matrix elements (a.u) between *i* and *j* NBO orbitals and  $q_i$  is the orbital occupancy.

The results of the second-order perturbation theory of the Fock Matrix [51] are presented in Table 3. The two largest values of energy (*E*(2)) are assigned to  $Lp(1)N12 \rightarrow \pi^*C10-C11$  (45.86 kcal. mol<sup>-1</sup>) and  $Lp(2)O1 \rightarrow \pi^*C2-O3$  (40.29 kcal. mol<sup>-1</sup>) interactions, this means that the two atoms N12 and O1 participate in the donor mesomeric relocation to stabilize the system. Other hyperactive-conjugative energy of  $Lp(2)O1 \rightarrow \pi^*C9-C4$  (32.64 kcal. mol<sup>-1</sup>) and  $Lp(2)O1 \rightarrow \pi^*C2-O1$  (34.06 kcal. mol<sup>-1</sup>) and the resonance in the aromatic ring of the 4-amino-2H-chromen-2-one fragment and in pyridine ring also plays an important role in stabilization of ligand structure.

### 3.3.5. Global indices of reactivity

The global reactivity descriptors are calculated according to the Koopmans theorem [52–55] by using HOMO and LUMO energy values of the geometry found by DFT calculations. These descriptors (electronic affinity (*A*), electronic ionization (*I*), chemical potential ( $\mu$ ), electronegativity (*X*), chemical hardness ( $\eta$ ), softness (*S*), electrophilicity index ( $\omega$ ) and nucleophilic index (*N*)) are used to estimate the capacity of the molecule to exchange electrons with the external medium. These parameters are listed with formulas in Table 4.

The global reactivity descriptors are calculated in order to confirm the nature of this crystal (electrophilic or nucleophilic). The obtained results indicate that the ligand present a hard character (chemical hardness) and the nucleophilic index value confirm that  $L_{TA}$  is more nucleophile, which promotes its complexation with biomolecules and metal ions. Therefore, the low value of chemical potential ( $\mu$ ), which is the additive inverse of the electronegativity ( $\chi$ ), may be explained by the fact that the tendency of the molecule to attract electrons is low.

The high value of  $\Delta E$  indicates a higher kinetic stability of 4-[(pyridin-3-ylmethyl) amino]-2H-chromen-2-one.

### 3.4. Mechanism

The geometries and energies of all stationary points: reagents, transition states (TS) and product ( $L_{TA}$ ) have been completely optimized and the vibration frequencies [56] have been calculated using B3LYP/6-31G+(d) model, implemented in Gaussian09 [57].

In order to study the kinetic and thermodynamic characteristics of the reaction mechanism of  $L_{TA}$  crystal formation given in

the previous scheme 1, calculations were performed and the results were reported in Table 5 and Fig. 8. We note that enthalpy and free enthalpy values are very low, indicating that the reaction is moderately exothermic. In addition, the formation mechanism of  $L_{TA}$  gives a high activation enthalpy value (59.58 kcal.mol<sup>-1</sup>). This significant value is explained by the fact that the formation reaction of the crystal is slow at 70 °C (crystals are formed after two weeks of evaporation).

We also note that the entropy variation of this chemical reaction is positive ( $\Delta S^\circ=0.0011255$ ), indicating an irreversible reaction. These results showed that the mechanism is well concerted (a single-step reaction) and the obtained product ( $L_{TA}$ ) is thermodynamically stable.

### 3.5. Thermodynamic properties of $L_{TA}$

The thermodynamic parameters were calculated using the DFT/B3LYP/6-31+G(d) level at temperature of 298.15 K and in solution phase (ethanol) of  $L_{TA}$  using PCM model. The computed parameters were tabulated in Table 5. The total energy of ligand was reported as −915.2642448 Hartrees. The sums of zero-point correction and thermal correlations to energies, enthalpies and Gibbs free energies with this calculated total energy value have been given sum of electronic and zero-point energy (−914.999196 Hartree/particle), sum of electronic and thermal energies (−914.979869 Hartree/particle), sum of electronic and thermal enthalpies (−914.978925 Hartree/particle) and sum of electronic and thermal free energies with −915.052821 Hartree/particle value. The Zero-point vibrational energy was calculated as 166.32076 kcal.mol<sup>-1</sup>. The calculated total value of entropy is 0.155528 kcal.mol<sup>-1</sup>.

### 3.6. Molecular docking studies

The molecular docking of SARS-CoV-2/Mpro-  $L_{TA}$  binding mode was simulated using AutoDock Tools Vina 1.5.6. This method allows explaining of the most energetically favorable binding sites of (4-[(pyridin-3-ylmethyl) amino]-2H-chromen-2-one) to SARS-CoV-2/Mpro receptor in terms of the binding energy and inhibition constant.

The 3D Main protease (Mpro)- $L_{TA}$  structure visualization was recorded using Discovery Studio 2020 and PyMOL software.

The aim of this study is to investigate the mode of interaction of  $L_{TA}$  with Main protease (Mpro), whose inhibition of this enzyme would prevent the virus from replication and therefore constitutes one of the potential anti-coronaviral strategies [57], which gives further clues to the prospect of developing SARS-CoV-2 drugs. Target protein (SARS-CoV-2/Mpro: Fig. 9a and Table S8) was retrieved from the Protein Data Bank (PDB: 6Y84) [58].

The interactions of (4-[(pyridin-3-ylmethyl) amino]-2H-chromen-2-one) with the protein are described in detail in Figs. 9 and 10. Indeed, the ligand ( $L_{TA}$ ) binds with SARS-CoV-2/Mpro via multiple hydrogen and Van der Waals bonding contacts, pi-pi T-shaped, carbon hydrogen and alkyl bonds, and also via hydrophobic contacts. Asn 142 form intermolecular conventional H-bond with  $L_{TA}$ , while His 163, Cys 145 and Met 165 form carbon hydrogen and pi-donor hydrogen bond, respectively. Whereas, Cys 44, Ser 46, Leu 141, Phe 140, Ser 44, His 172, Glu 166, Gly 143, Thr 26, Leu 27 and Thr 25 form Van der Waals interactions with inhibitor ligand. In addition, Met 49 and Cys 145 give pi-alkyl bonds and His 41 gives pi-pi T-shaped bond with  $L_{TA}$  (Fig. 9b).

Fig. 10a reports 3D-illustration of the H-bond interactions between the inhibitor ( $L_{TA}$ ) and the amino acids of SARS-CoV-2/Mpro. The region occupied by Asn 142 is electron acceptors (in green)

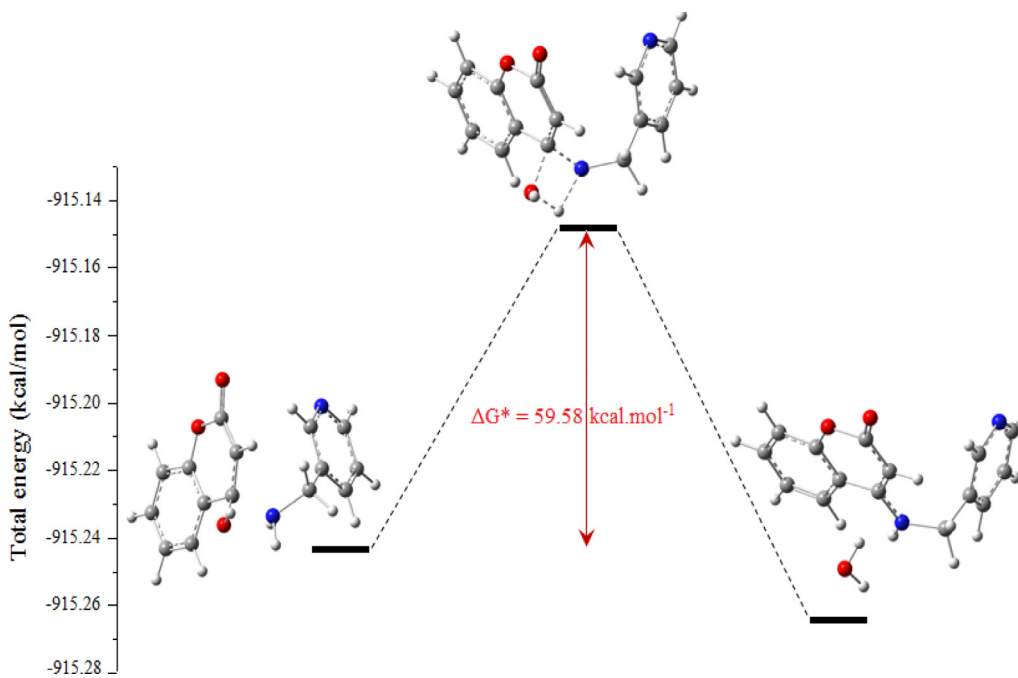


**Fig. 8.** Energetic diagram of the formation of ligand L<sub>TA</sub> obtained by DFT.

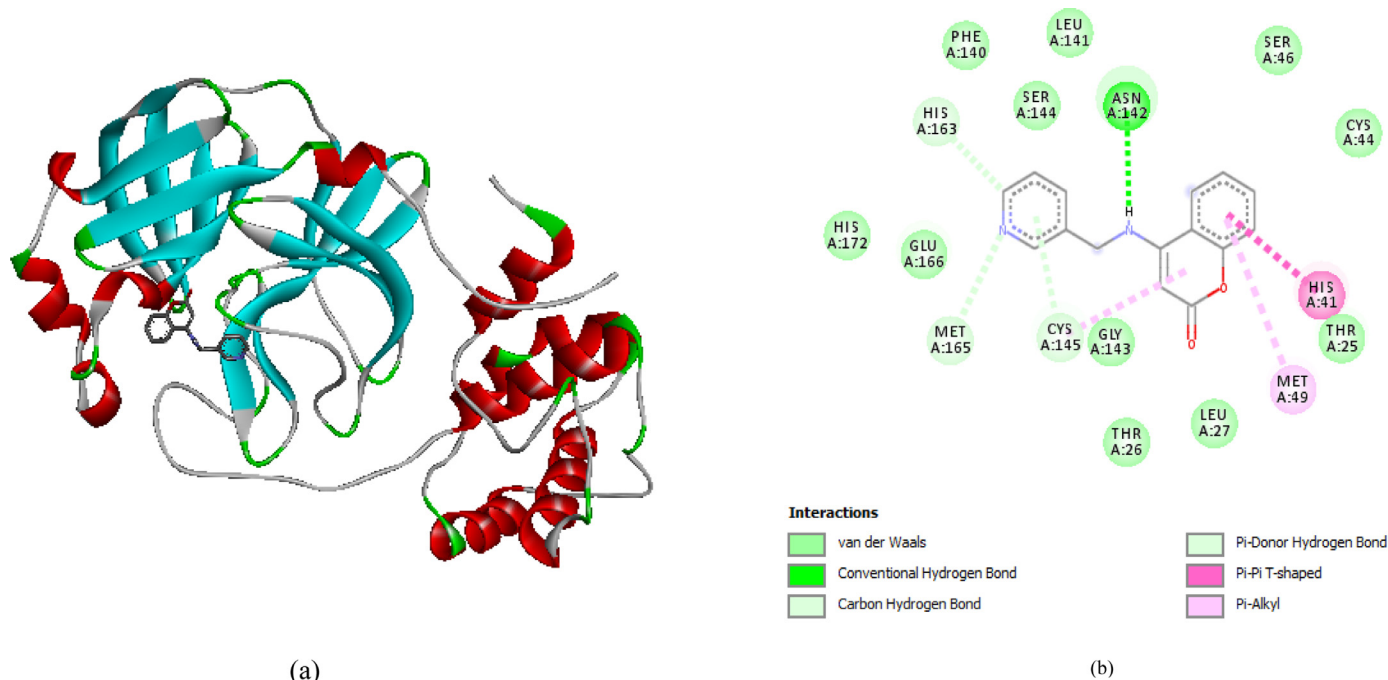


**Fig. 9.** The representative structure of SARS-CoV-2/Mpro- L<sub>TA</sub> complex: (a) SARS-CoV-2/Mpro is represented in Ribbon drawings, L<sub>TA</sub> and binding sites are represented in stick and in color (red and blue), respectively; (b) 2D diagram of the interaction of L<sub>TA</sub> with SARS-CoV-2/Mpro from AutoDock Tools Vina 1.5.6. docking.

and these occupied by other amino acids are electron donors (in purple).

Fig. 10b shows that the oxygen and sulfur of the C = O and S-H groups of the amino acids (Asn 142 and Cys 145) are in close proximity 2.12 Å (conventional H-bond) and 4.41 Å (pi-donor H-bond) to L<sub>TA</sub>. The aromatic ring of the ligand is in close to His 41 with the distance of 4.28 Å and forms pi-pi T-shaped interaction.

The interpolated charge (electrostatic charge) contour map (Fig. 10c) shows significant increase of negative charge in the red contour region, leading to increased activity with L<sub>TA</sub>.

The SARS-CoV-2/Mpro also displayed few hydrophobic contacts mediated by the aliphatic amino acids (Fig. 10e), and it is moderately basic (in blue) (Fig. 10f).

The 3D structure visualizations (Fig. 10a, b-f) showed that SARS-CoV-2/Mpro envelopes the ligand, this creates a strong cohesive environment and stability of the formed complex. The enclosed SARS-CoV-2/Mpro-L<sub>TA</sub> complex should be inactive against cells in the human body.

Through docking simulation, various physical parameters were obtained. The binding energy calculated for L<sub>TA</sub>- SARS-CoV-2/Mpro

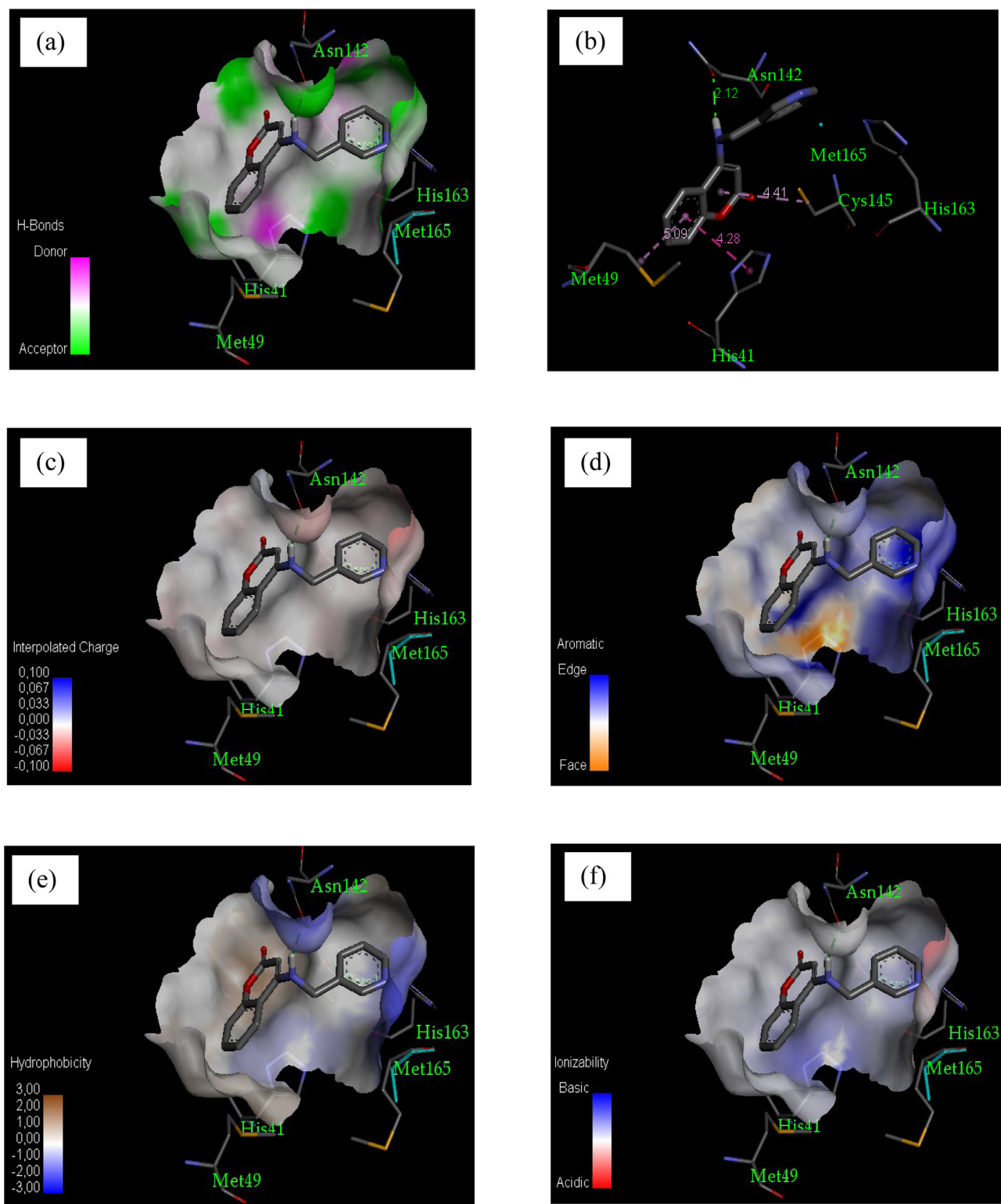


**Fig. 10.** Docking studies of  $L_{TA}$  binding-active site of SARS-CoV-2/Mpro with various bonding interactions. (a) H-bond; (b) Hydrogen bonds (colored dashed lines, distances are in Å units) between SARS-CoV-2/Mpro and the inhibitor (ligand); (c) Interpolated charge; (d) Aromatic; (e) Hydrophobic and (f) Ionizability distributions.

complex ( $-7.03 \text{ kcal. mol}^{-1}$ ), intermolecular energy ( $-7.93 \text{ kcal. mol}^{-1}$ ), Van der Waals/H-bond/desolvation energy ( $-7.89 \text{ kcal. mol}^{-1}$ ) and inhibition constant ( $6.98 \mu\text{M}$ ) show active  $L_{TA}$  molecule with the ability to inhibit SARS-CoV-2. This high binding affinity is as linked with the presence of four H-bonds with the amino acids Asn 142, His 163, Met 165 and Cys 145.

In summary, the binding mode demonstrated in this study therefore provides a useful clue to understanding the possible molecular basis and interaction of this inhibitor ( $L_{TA}$ ) with SARS-CoV-2.

Comparing the results found in this work with those reported in the literature, we find that both molecules chloroquine and

hydroxychloroquine present lower binding energy (chloroquine:  $-5.9 \text{ kcal. mol}^{-1}$ ; hydroxychloroquine:  $-6.0 \text{ kcal. mol}^{-1}$ ) and inhibition constants (chloroquine:  $30.8 \mu\text{M}$ ; hydroxychloroquine:  $22.9 \mu\text{M}$ ) [27].

## 4. Conclusion

In the present work, synthesis, spectroscopic characterization (ATR, NMR and UV-Visible), crystal structure of 4-[(pyridin-3-ylmethyl) amino]-2H-chromen-2-one ( $L_{TA}$ ) were reported. Density functional theory (DFT) has been applied to support the experimental results and to report the various molecular properties like HOMO-LUMO energies and gap, NBO and MEP properties, global reactivity descriptors, kinetic and thermodynamic parameters of  $L_{TA}$ . In addition, molecular docking was used to investigate the mode of interaction of  $L_{TA}$  with SARS-CoV-2/Mpro.

The results of single crystal X-ray diffraction analysis show that this compound crystallized in monoclinic system with space group  $P\ 2_1$  ( $Z = 4$ ).

The natural bond order (NBO) analysis and the molecular MEP map showed that the O1, O3, N12 and N18 sites are more favored for electrophilic attacks, but the H12 site is more favored for nucleophilic attacks. The stabilization energy E(2) showed that N12 and O1 participate to stabilize  $L_{TA}$ . The global reactivity descriptors obtained indicate that the ligand is more nucleophile and presents a hard character.

The kinetic and thermodynamic parameters of  $L_{TA}$  showed that the formation mechanism of the crystal is moderately exothermic with a high activation enthalpy. These results indicate that the synthetic product ( $L_{TA}$ ) is thermodynamically stable.

The interaction of (4-[(pyridin-3-ylmethyl) amino]-2H-chromen-2-one) with SARS-CoV-2/Mpro revealed that the ligand ( $L_{TA}$ ) binds to SARS-CoV-2/Mpro via multiple bonding contacts. Through docking simulation, the binding energy calculated for SARS-CoV-2/Mpro-  $L_{TA}$  complex and inhibition constant showed active  $L_{TA}$  molecule with the ability to inhibit SARS-CoV-2 (Covid-19).

## Declaration of Competing Interest

The authors declare that they have no known competing financial interests or personal relationships that could have appeared to influence the work reported in this paper.

## CRediT authorship contribution statement

**Chafia Ait-Ramdane-Terbouche:** Conceptualization, Formal analysis, Software, Writing - original draft. **Hasnia Abdeldjebar:** Funding acquisition, Software, Data curation. **Achour Terbouche:** Conceptualization, Methodology, Writing - original draft, Supervision, Validation, Writing - review & editing. **Houria Lakhdiri:** Validation, Formal analysis, Data curation. **Khaldoun Bachari:** Funding acquisition, Data curation, Writing - review & editing. **Thierry Roisnel:** Formal analysis, Validation. **Didier Hauchard:** Formal analysis, Methodology, Validation.

## Acknowledgements

The authors would like to acknowledge the MESRS Algerian Ministry and Directorate-General for Scientific Research and Technological Development (Algeria) for supporting the present research.

## Supplementary materials

Supplementary material associated with this article can be found, in the online version, at doi:10.1016/j.molstruc.2020.128918.

## References

- [1] X.W. Wu, W. Wei, X.W. Yang, Y.B. Zhang, W. Xu, Y.F. Yang, G.Y. Zhong, H.N. Liu, S.L. Yang, Molecules 22 (2017) 935.
- [2] Y. Shokoohinia, F. Jafari, Z. Mohammadi, L. Bazvandi, L. Hosseinzadeh, N. Chow, P. Bhattacharyya, M.H. Farzaei, A.A. Farooqi, S.M. Nabavi, M.B. Yerer, A. Bishayee, Nutrients 10 (2018) 36.
- [3] Y. Wang, S.L. Duan, Q.Y. Zhang, W. Cheng, H. Liang, Chin. Tradit. Herbal Drugs 45 (2014) 333–336.
- [4] J.-C. Sun, J.-L. Li, C.-B. Ji, Y.-Y. Peng, X.-P. Zeng, Tetrahedron 76 (2020) 130852.
- [5] E.H. Maleki, A.R. Bahrami, H. Sadeghian, M.M. Matin, Toxicol. in Vitro 63 (2020) 104745.
- [6] F.R. Chang, P.S. Li, R.H. Liu, H.C. Hu, T.L. Hwang, J.C. Lee, S.L. Chen, Y.C. Wu, Y.B. Cheng, J. Nat. Prod. 81 (2018) 1534–1539.
- [7] N.H. Ouf, Y.A. Selim, M.I. Sakran, A.S.B. El-din, Med. Chem. Res. 23 (2014) 1180–1188.
- [8] M. Trkovnik, M. Cacic, J. Rizvani, Coumarin derivative as antiviral agent, pharmaceutical composition thereof, its preparation and use (International Publication Number Patent: WO 2016/156888 A1; International Application Number Patent: PCT/HR2016/000005), 2016. <https://patentimages.storage.googleapis.com/3d/a8/0c/a901c706d6e603/WO2016156888A1.pdf>.
- [9] E.Y. Ahmed, N.A. Abdel Latif, M.F. El-Mansy, W.S. Elserwy, O.M. Abdelhafez, Bioorg. Med. Chem. (2020) 115328.
- [10] A.S. Haque, V. Singh, D. Katiyar, M.T.A. Khan, V. Tripathi, H. El Enshasy, M. Pasupuleti, B.N. Mishra, Process Biochem. 87 (2019) 138–144.
- [11] M. Rajabi, Z. Hossaini, M.A. Khalilzadeh, S. Datta, M. Halder, S.A. Mousa, J. Photochem. Photobiol. 148 (2015) 66–72.
- [12] M. Jun, A.F. Bacay, J. Moyer, A. Webb, D. Carrico-Moniz, Bioorg. Med. Chem. Lett. 24 (2014) 4654–4658.
- [13] H.A. El-Sherief, G.E.A. Abuo-Rahma, M.E. Shoman, E.A. Beshr, R.M. Abdel-baky, Med. Chem. Res. 26 (2017) 3077–3090.
- [14] N. Lv, M. Sun, C. Liu, J.B. Li, Bioorg. Med. Chem. Lett. 27 (2017) 4578–4581.
- [15] L. Musajo, G. Rodighiero, Acta Derm. Venereol. 47 (1967) 298–303.
- [16] F.A. Mir, Optik (Stuttg.) 126 (2015) 24–27.
- [17] O. Zaneva, I. Manolov, N. Danchev, in: Toxicological and Pharmacological Investigations of Newly Synthesized Derivatives of 4-hydroxycoumarin, vol. LII, Pharmacia, Sofia, 2005, pp. 85–89.
- [18] V.D. Kancheva, P.V. Boranova, J.T. Nechev, I.I. Manolov, Biochimie 92 (2010) 1138–1146.
- [19] A.K. Patel, N.H. Patel, M.A. Patel, C.V. Patel, D.I. Synthetic Commun 44 (2014) 1881–1887.
- [20] J. Liu, J. Li, X. Yuan, W. Wang, J. Xue, Photodiagn. Photodyn. Therapy 13 (2016) 341–343.
- [21] K.V. Sashidhara, A. Kumar, M. Kumar, S. Singh, M. Jain, M. Dikshit, Bioorg. Med. Chem. Lett. 21 (2011) 7034–7040.
- [22] W. Lu, F. Huang, H. Hua, J. Chen, S. Qiu, F. Zhao, J. Shi, L. Xu, S. Yang, X. Chi, J. Mol. Struct. 1192 (2019) 115–121.
- [23] H.Y. Lin, G. Song, Y. Tian, J.F. Lin, X. Wang, G.C. Liu, Transition Met. Chem. 43 (2018) 185–192.
- [24] S.I. Ivlev, M.R. Buchner, A.J. Karttunen, F. Kraus, J. Fluorine Chem. 215 (2018) 17–24.
- [25] J. China coronavirus, cases surge as official admits human to human transmission, British Med. J. Group (2020).
- [26] D.S. Hui, T. Madani, F. Ntoumi, R. Kock, O. Dar, G. Ippolito, T. Mchugh, Z. Memish, C. Drosten, A. Zumla, The continuing 2019-nCoV epidemic threat of novel coronaviruses to global health – The latest 2019 novel coronavirus outbreak in Wuhan, Int. J. Infect. Dis. 91 (2020) 264–266.
- [27] M.D.L. de Oliveira, K.M.T. de Oliveira, Comparative Computational Study of SARS-CoV-2 Receptors Antagonists from Already Approved Drugs, ChemRxiv (2020), doi:[10.26434/chemrxiv.12044538.v1](https://doi.org/10.26434/chemrxiv.12044538.v1).
- [28] C.B. Aguirre-Pranzoni, G.I. Furque, C.E. Ardanaz, A. Pacciaroni, V. Sosa, C.E. Tonn, M. Kurina-Sanz, Arkivoc 7 (2011) 170–181.
- [29] E.V. Stoyanov, I.C. Ivanov, Molecules 9 (2004) 627–631.
- [30] S.K. Karagiosov, I.C. Ivanov, B.I. Iliev, Molecules 4 (1999) M126.
- [31] F.A. Mohammed, S. Yehia, S.H. Ali, Physica B: Condensed Matter 407 (2012) 2486–2489.
- [32] C. Lee, W. Yang, R.G. Parr, Phys. Rev. B 37 (1988) 785.
- [33] M.J. Frisch, G.W. Trucks, H.B. Schlegel, G.E. Scuseria, M.A. Robb, J.R. Cheeseman, G. Scalmani, V. Barone, B. Mennucci, G.A. Petersson, H. Nakatsuji, M. Caricato, X. Li, H.P. Hratchian, A.F. Iamaylov, J. Bloino, G. Zheng, J.L. Sonnenberg, M. Hada, M. Ehara, K. Toyota, R. Fukuda, J. Hasegawa, M. Ishida, T. Nakajima, Y. Honda, O. Kitao, H. Nakai, T. Vreven, J.A. Montgomery jr, J.E. Peralta, F. Ogliaro, M. Bearpark, J.J. Heyd, E. Brothers, K.N. Kudin, V.N. Staroverov, R. Kobayashi, J. Normand, K. Raghavachari, A. Rendell, J.C. Burant, S.S. Liyengar, J. Tomasi, M. Cossi, N. Rega, J.M. Millam, M. Klene, J.E. Knox, J.B. Cross, V. Bakken, C. Adamo, J. Jaramillo, R. Gomperts, R.E. Stratmann, O. Yazyev, A.J. Austin, R. Cammi, C. Pomelli, J.W. Ochterski, R.L. Martin, K. Morokuma, V.G. Zakrzewski, G.A. Voth, P. Salvador, J.J. Dannenberg, S. Dapprich, A.D. Daniels, O. Farkas, J.B. Foresman, J.V. Ortiz, J. Cioslowski, D.J. Fox, Gaussian 09, Revision A. 1 Gaussian Inc., Wallingford CT, 2009.
- [34] O. Lin-Vien, N.B. Cothup, W.G. Fateley, J.G. Graselli, The Handbook of Infrared and Raman Characteristic Frequencies of Organic Molecules, Academic Press, Boston, 1991.

- [35] M. Diem, *Introduction to Modern Vibrational Spectroscopy*, Vol. 1, Wiley, New York, 1993.
- [36] Y. Sert, S. Sreenivasa, H. Doqan, N.R. Mohan, P.A. Suchtan, F. Ucun, *Spectrochem. Acta Part A: mol. Biomol. Spectrosc.* 130 (2014) 96–104.
- [37] K. Wolinski, J.F. Hilton, P. Pulay, *J. Am. Chem. Soc.* 112 (1990) 8251–8260.
- [38] L. Pauling, the resonating-valence-bond theory of superconductivity: crest superconductor and through superconductors, *Proc. Natl. Acad. Sci. United States of America* 60 (1968) 59.
- [39] M. Alam, M.J. Alam, S.A.A. Nami, D.-U. Lee, M. Azam, S. Ahmad, *J. Mol. Struct.* 1108 (2016) 411–426.
- [40] J. Liu, J.M. Herbert, *J. Chem. Phys.* 143 (2015) 034106.
- [41] E. Runge, E.K. Gross, *Phys. Rev. Lett.* 52 (1984) 997.
- [42] A. Terbouche, C. Ait-Ramdane-Terbouche, Z. Bendjilali, H. Berriah, H. Lakhdari, D. Lerari, K. Bachari, D. Mezaoui, N.E.H. Bensiradj, J.-P. Guegan, D. Hauchard, *Spectrochim. Acta Part A: Mol. Biomol. Spectrosc.* 205 (2018) 146–159.
- [43] K. Jug, Z.B. Maksic, part 3, Springer, Berlin, 1991, pp. 29–233.
- [44] E. Scrocco, J. Tomasi, *Adv. Quantum Chem.* 11 (1979) 115.
- [45] F.J. Luque, J.M. Lopez, M. Orozco., *Theor. Chem. Acc.* 103 (2000) 343–345.
- [46] I. Sidir, Y.G. Sidir, M. Kumalar, E. Tasal, *J. Mol. Struct.* 964 (2010) 134–151.
- [47] J. Gasteiger, S. Fliszar, in: *Charge Distribution and Chemical Effets*, 88, Springer Verlag, Berlin, Heidelberg, New York, Tokyo, 1984, pp. 686–687. 1983. 205 Seitrn, Preis: DM 115-Berichte der Bunsesellschaft fur physikalische Chemie.
- [48] M. Amalanathan, V.K. Rastogi, I.H. Joe, M.A. Palafox, R. Tomar, *Spectrochim. Acta Part A: mol. Biomol. Spectrosc.* 78 (2011) 1437–1444.
- [49] D.W. Schwenke, D.G. Truhlar, *J. Chem. Phys.* 82 (1985) 2418–2427.
- [50] M. Gutowski, G. Chalasinski, *J. Chem. Phys.* 98 (1993) 4728–4738.
- [51] E.S. Kryachko, Neutral blue-shifting and blue-shifted hydrogen bonds, in: *Hydrogen Bonding- New Insights*, Springer, 2006, pp. 293–336.
- [52] S. Sagdinc, H. Pir, *Spectrochim. Acta, Part A: Mol. Biomol. Spectrosc.* 73 (2009) 181–187.
- [53] D.F.V. Lewis, C. Loannides, D.V. Parke, *Xenobiotica* 24 (1994) 401–408.
- [54] R.G. Parr, R.A. Donnelly, M. Levy, W.E. Palke, *J. Chem. Phys.* 68 (1978) 3801–3807.
- [55] R.G. Parr, L.V. Szentpaly, S. Liu, *J. Am. Chem. Soc.* 121 (1999) 1922–1924.
- [56] Y. Zhao, N.E. Schultz, D.G. Truhlar, *J. Chem. Theory Comput.* 2 (2006) 364–382.
- [57] D.L.L. Zhang, X. Sun, K. Rox, R. Hilgenfeld, *Biorxiv* (2020) Preprint server, doi:10.1101/2020.02.17.952879.
- [58] C.D. Owen, P. Lukacik, C.M. Strain-Damerell, A. Douangamath, A.J. Powell, D. Fearon, J. Brandao-Neto, A.D. Crawshaw, D. Aragao, M. Williams, R. Flraig, D.R. Hall, K.E. McAuley, M. Mazzorana, D.I. Stuart, F. von Delft, M.A. Walsh, SARS-CoV-2 main protease with unliganded active site (2019-nCoV, coronavirus disease 2019, COVID-19, 2020. doi: 10.2210/pdb6Y84/pdb.